Available online at www.sciencedirect.com
ScienceDirect
Advances in Space Research 47 (2011) 1758–1776
ADVANCES IN SPACE RESEARCH (a COSPAR publication)
www.elsevier.com/locate/asr

Propagation of plasma bubbles observed in Brazil from GPS and airglow data

J.S. Haase [a], T. Dautermann [b,*], M.J. Taylor [c], N. Chapagain [c], E. Calais [a], D. Pautet [c]

[a] Purdue University, Department of Earth and Atmospheric Sciences, West Lafayette, Indiana, USA
[b] German Aerospace Center (DLR), Department of Communication and Navigation, Oberpfaffenhofen, 82253 Wessling, Germany
[c] Utah State University, Department of Physics, Logan, Utah, USA

Received 20 December 2009; received in revised form 20 September 2010; accepted 24 September 2010
Available online 8 October 2010

Abstract

Equatorial spread-F is a common occurrence in the equatorial ionosphere that is associated with large variations in plasma density that often cause scintillation and interference in communication signals. These events are known to result from Rayleigh–Taylor instability, but the day-to-day variability of their occurrence is not well understood. The triggering mechanism of plasma depletions is still a matter of debate, but may be linked to gravity waves that under favorable conditions propagate to the middle atmosphere. Understanding the triggering of ESF was the focus of the SpreadFEx campaign near Brasilia, Brazil in 2005. The campaign provided co-located airglow and GPS observations to study the onset of plasma depletions and their evolution as they traversed the region. Comparisons between the 630.0 nm airglow data and GPS data demonstrate the ability of the compact dual frequency GPS array to detect the plasma bubbles and retrieve reliable propagation characteristics of the depletions. In this case study, a plasma depletion was detected and moved over the array at velocities of 85–110 m/s, slowing as it moved towards the east. Correlation of consecutive airglow images gives consistent estimates of the eastward drift over the same time period. Mapping the airglow data to the GPS line-of-sight geometry allows direct comparison and reveals a resolvable westward tilt of the plasma depletion that may be due to vertical shear. The uniqueness of this study is the ability to resolve locally the characteristics of the plasma depletion without relying on assumptions about the mapping of the depletion along magnetic field lines to large latitudinal distances. It presents new information for understanding ESF development and the development of depletions strong enough to produce scintillation.
© 2010 COSPAR. Published by Elsevier Ltd. All rights reserved.

Keywords: Total electron content; Plasma bubbles; Airglow; GPS remote sensing

1. Introduction

The post-sunset enhancement of upward plasma drift has been shown to be a key component in the generation of equatorial spread-F (ESF) (Basu et al., 1996). The eastward electric field generated in the ionospheric E region during the day causes a vertical $\mathbf{E} \times \mathbf{B}$ drift of F region plasma at the equator. As solar ionization in the E layer decreases in the late afternoon and the ion density decreases, the F region dynamo starts to dominate. The post-sunset enhancement of the electric field is caused by this influence from the F region dynamo in conjunction with the conductivity gradient across the solar terminator. With an enhanced electric field, the vertical plasma drift is enhanced and typically drives the plasma to altitudes of 500 km or greater. It rises until pressure gradients are large enough that it diffuses along magnetic field lines towards the tropics. Recombination is slow at these altitudes, so regions of enhanced density often persist past local midnight, to form the equatorial anomaly at $\pm 15°$ of the magnetic equator. After sunset, the lower ionosphere rapidly decays, forming a steep density gradient at the base of the raised F-region, and creating the conditions for a

* Corresponding author. Tel.: +49 8153 282809.
E-mail address: thomas.dautermann@dlr.de (T. Dautermann).

0273-1177/$36.00 © 2010 COSPAR. Published by Elsevier Ltd. All rights reserved.
doi:10.1016/j.asr.2010.09.025

gravitational Rayleigh–Taylor instability. A perturbation at the base of the F-region, such as that caused by a gravity wave, for example, can lead to growth of the instability, resulting in the formation of plasma bubbles, that is, structures with depleted plasma density, that produce ESF (Abdu, 2001; Abdu et al., 2009; Huang and Kelley, 1996a,b; Kelley, 1989).

The general characteristics of ESF and its large scale variability are relatively well understood. Depletions generally extend poleward along the magnetic flux tube into the Appleton anomaly regions, typically 100–200 km in the east–west direction, and drift towards the east at approximately 50–150 m/s (Garcia et al., 2000a; Kelley, 1989). Seasonally, scintillations in UHF transmissions associated with ESF occur at a given longitude at the time of year when the solar terminator is closely aligned with the magnetic flux tubes (Tsunoda, 1985). There have been studies that associate ESF occurrence with times when the latitude of the equatorial anomaly crests are furthest from the equator (Valladares et al., 2001; Whalen, 2001), and also studies suggesting that ESF preferentially occurs when the Appleton anomaly crests are symmetric. ESF is suppressed when the crests are asymmetric, due to meridional transequatorial winds changing the Pedersen conductivity and suppressing the growth of the Rayleigh–Taylor instability (Maruyama, 1988; Maruyama and Matuura, 1984). The depletions develop a westward tilt due to a vertical shear in the horizontal drift velocity caused by the height dependence in the ratio of the equatorial F-region and off-equatorial E-region Pedersen conductivities (Mendillo and Tyler, 1983; Zalesak et al., 1982). Narrow-field airglow images have shown vertical shear in the depletions as they move eastward, with the tilt increasing with time over the course of the evening (Makela and Kelley, 2003). 630.0 nm airglow imagery, which is sensitive to heights around 250–280 km, tends to show a decrease in eastward drift velocity with local time, consistent with this trend (Terra et al., 2004). Despite these significant advances in the understanding of the characteristics of equatorial spread-F, the day-to-day variability remains difficult to predict in terms of the onset time and location over the course of an evening.

This study investigates features of an individual ESF event at the local scale to recover characteristics such as height, drift, and tilt of the plasma bubbles from a combined Global Positioning System (GPS) total electron content (TEC) (Klobuchar, 1985) and airglow dataset. The objective is to investigate the evolution of the plasma bubbles where there is an unambiguous correlation of airglow and GPS features so that characteristics evident in GPS signals can described and the use of small GPS arrays for detection can be expanded. Historically, the principal techniques for probing the post-sunset ionosphere to observe equatorial spread-F have been radar, ionosondes and airglow images, however observations of integrated electron content and scintillation from satellite signals are now used to observe these features. The small aperture multi-station TEC approach used in this study extends the observational techniques at our disposal for studying equatorial spread-F, with the advantage that the GPS measurements are not affected by clouds and can be made in moonlight. In Section 2 we review recent advances in using HF to UHF satellite signals to study ESF and focus in particular on those that use GPS to sample the equatorial ionosphere. In Section 3 we describe the dataset used in this study. Section 4 presents the GPS data processing method and GPS estimates of eastward drift of the depletions. Section 5 compares the detection of depletions from GPS data with airglow data. Section 6 compares and interprets drift velocity estimates made from airglow and GPS data. A discussion of the results and major conclusions are provided in Section 7.

2. Review of the use of GPS for studying ESF

Ionospheric irregularities, and in particular ESF, cause amplitude and phase scintillations at frequencies from HF to UHF, within approximately 15° of the geomagnetic equator. Scintillation is typically quantified using the S4 index, which has been defined as the standard deviation of the signal power sampled at high frequency divided by its average, usually over 1 min intervals (Yeh and Liu, 1982). 250 MHz signals from geostationary satellites have been used to study scintillation. These signals were recorded on two receivers with small horizontal offset in the east–west direction, then zonal velocities were determined by cross-correlating the S4 index time series (Basu et al., 1996; Valladares et al., 1996). 250 MHz signals reveal scintillation from 1 km scale ionospheric irregularities.

Since the deployment of many permanent GPS stations worldwide over the last decade, GPS signals have been used to study the ionosphere using both scintillation and the integrated electron content. GPS signals can be severely affected by scintillations due to plasma irregularities, especially in the equatorial regions. In one study, the zonal drift of irregularities was measured by cross-correlating the signal power at two GPS receivers (de Paula et al., 2002; Kil et al., 2002), however the velocity was not determined accurately enough to provide conclusive evidence that it represented depletion eastward drift. In another study, two single frequency GPS receivers were deployed near the VHF coherent backscatter radar at São Luis, Brazil, to observe equatorial spread-F using scintillation (Rodrigues et al., 2004). These observations showed consistency with the observed zonal velocities of 200 m/s observed in radar irregularities for deep vertical plume structures, but not for F region bottom side irregularities detected by the radar.

One of the earliest GPS studies made qualitative comparisons of variations in integrated electron content (IEC, sometimes also called total electron content or TEC) with observations of spread-F in the equatorial ionosphere at Kwajalein (Kelley et al., 1996). IEC fluctuations have also been compared to the S4 index from GPS

receivers, but their timing does not uniquely correlate because IEC observations typically retrieved from GPS data sampled at 30 s do not measure the small scale features at the Fresnel scale seen in the S4 amplitude (Beach and Kintner, 1999).

GPS data have been combined with other types of data in studies attempting to link phenomena observed at larger continental scales. Comparisons of GPS phase fluctuations in total electron content at one site in Arequipa with digisonde observations at Jicamarca over a year yielded a correlation of lower amplitude GPS phase fluctuations with the appearance of spread-F on ionograms and a correlation of very high amplitude GPS phase fluctuation with topside F-layer plasma bubbles (Chen et al., 2006). Studies using data from a network of widely spaced permanent sites in South America investigated the relationship between GPS IEC fluctuations and the location of the Appleton anomaly peaks (Mendillo et al., 2000).

Previous studies of GPS data combined with airglow have also led to insight into the variability of ESF. Airglow measured at 630.0 nm results from charge exchange of O^+ with O_2 followed by dissociative recombination of O_2^+ to produce $O(^1D)$ (Mendillo and Baumgardner, 1982). The intensity of airglow depends on the O^+ and O^2 altitude profiles between the lower edge of the bottomside F layer and about 350 km. Weber et al. (1996) made qualitative comparisons between depletions imaged with 630.0 nm all-sky airglow and scintillations measured by GPS. That study found evidence for poleward extension of depletions, assuming a direct mapping along the magnetic field line between stations at lower latitudes and observations at higher altitudes above the airglow imager. Seasonal variations in equatorial plasma bubbles were studied in Hawaii using a combined GPS and airglow dataset (Makela et al., 2004). Plasma bubbles were also documented using airglow and TEC measurements as high as 28° magnetic latitude. At these latitudes ionospheric irregularities were observed simultaneously in 630 nm airglow and GPS TEC (Martinis and Mendillo, 2007).

Additionally, Makela et al. (2004) used airglow images in conjunction with IEC calibration. Garcia et al. (2000b) used the two data sources to measure mesoscale ionospheric structures and found co-located, untilted depletions over Arecibo, Puerto Rico. Kelley et al. (2003) report on combined measurements taken at Hawaii in February 2002, where scintillations were so strong that their GPS receiver failed during the time, when the depletion passed through the line of sight.

Use of one GPS scintillation monitor (Beach and Kintner, 1999) and one dual frequency GPS receiver to measure TEC produced a similar seasonal pattern to that retrieved from the airglow imagers for detected plasma depletions, however the study did not provide estimates of drift velocities. A latitudinal array of GPS receivers was used to retrieve the time delays of signals in the S4 scintillation index between sites (Valladares et al., 2004). These were used to interpret the altitudinal extent of the depletions, and their tilt. A comparison of the S4 index from Wide Area Augmentation Satellite (WAAS) signals at one site with observations from a collocated 630 nm airglow imager suggested that scintillation strength tends to be largest on the plasma bubble walls (Ledvina and Makela, 2005).

Several of the aforementioned studies assumed that the depletion maps along magnetic flux tubes so that observations at 350 km altitude at sites far from the equator could be mapped to higher altitudes at the equator, and that this projection could be used to estimate plasma drift and tilt from stations at large latitudinal separations. While in general this can be done, the mapping depends on the ratio of Pedersen conductivities in the E and F region, which are not necessarily well known.

We seek to use a localized array of GPS receivers to determine the drift velocity and use the data in combination with airglow to constrain the tilt of the depletion or equivalent shear in the drift velocities. The aforementioned studies that concentrate on the detection of plasma bubbles through scintillation rely on the assumption that the small scale (~400 m) irregularities occur on the edge of the larger scale plasma bubbles. The scintillation observations from one receiver compared with airglow (Ledvina and Makela, 2005), for example, show a time delay that is hypothesized to be related to the difference in height of observations and thickness of the scintillation layer, however the results are not conclusive. We investigate whether array measurements of GPS integrated electron content give estimates of plasma depletion characteristics that are comparable to airglow observations, not only in terms of timing but also in terms of scale and drift velocity.

3. Data

The SpreadFEx campaign was designed to observe equatorial spread-F phenomena, and in particular plasma bubbles, their altitudinal extent and structure, and attempt to link them with gravity wave activity. The campaign took place in eastern and central Brazil during moon down conditions from September to November 2005 (Fritts et al., 2009). The campaign included observations from VHF radar, meteor radars, digisondes, airglow imagers and GPS receivers (Fig. 1). This paper deals with observations of equatorial spread F during the campaign from the GPS receivers and the 630.0 nm optical imager deployed at Fazenda Isabel in central Brazil. It concerns the first step of linking GPS receiver signals with plasma bubbles, as a prerequisite to future work linking GPS signals with precursory gravity waves.

Five temporary GPS stations were set up in a small network surrounding the all sky imager with an approximate spacing of 100 km between sites. The temporary sites were set up at Fazenda Isabel, São João de Aliança (FAZ1), Parco Nacional, Ibama Alto Paraiso (ALPA), Alvorado do Norte (ALVO), Flores de Goias (FLOR) and Teresina de Goias (TERE) with the exact coordinates given in

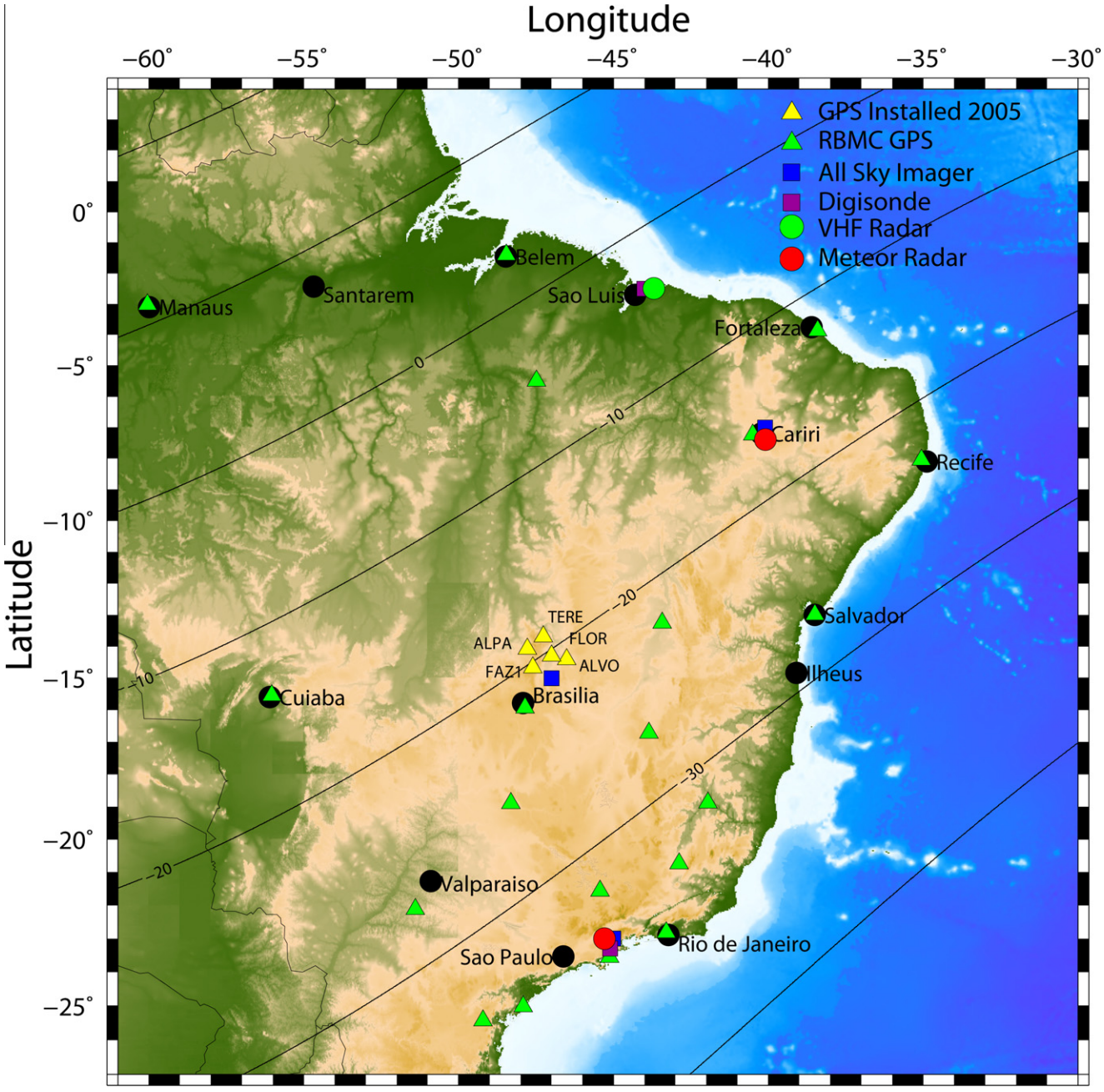

Fig. 1. GPS and airglow imager site locations, along with other observation sites recording data during the SpreadFEx campaign. Lines of constant magnetic inclination are shown.

Table 1. The temporary array was deployed during the time period 27 September through 10 November 2005. The dual frequency GPS receivers recorded phase and signal-to-noise ratio at a 30 s sampling interval on L1 and L2 frequencies. Power and logistical problems prevented obtaining a continuous dataset throughout the whole campaign, however at three sites very good recordings were made on 12 days.

The Utah State University all-sky airglow imager located at Fazenda Isabel is capable of sequential imaging the near infrared (NIR) hydroxyl (OH) Meinel broad band emission (710–930 nm), the OI (557.7 nm) green line emission and the OI 630.0 nm red line emission with a cadence of ~5 min. Typical exposure times are 120 s for each OI line emissions and 15 s for the OH emission. Image measurements were made during two consecutive moon down periods from 25 September to 10 October and from 23 October to 8 November 2005. Emissions at 630.0 nm are the result of a two-step chemical reaction involving O^+ and O_2^+ and occur slightly below the peak of electron density in the ionosphere centered at ~280 km (Tinsley et al., 1973). The OH and 557.7 nm emissions originate in the mesosphere centered at ~87 and 96 km, respectively, but there is some thermospheric contribution to 557.7 nm emis-

Table 1
Locations of the GPS sites.

Site	Longitude	Latitude
ALPA	−47.788579	−14.073832
TERE	−47.264411	−13.696128
FAZ1	−47.602838	−14.665781
ALVO	−46.506171	−14.406658
FLOR	−47.03427	−14.49657

sions at low-latitudes. The camera is a well-proven field instrument and uses a sensitive back-thinned solid state 1024 × 1024 pixel charge couple device (CCD) array. Data are 2 × 2 binned on the chip resulting in a horizontal resolution of 0.5 km (Taylor and Bishop, 1995; Taylor et al., 1997). Fig. 2 shows an example of the 630.0 nm airglow data exhibiting extensive matured depletions aligned parallel to magnetic north–south. The measurements were obtained on September 30 – October 1, 2005, and depletions were observed propagating eastward for 4.8 h from 23:00 to 03:40 UTC over Fazenda Isabel.

On the night of October 1–2, the all sky image camera was operated in a higher temporal mode where sequential images of the mesospheric OH and 630 nm OI emission structure were obtained every 2.4 min. Data were obtained from 22:12 to 08:00 UTC (19:12 to 05:00 LT). On this night, the plasma depletions were not detected until ~00:15 UTC. Depletions were first detected to the northwest and a single plasma depletion entered the field of view to the west at ~00:30 UTC. This feature moved eastward and evolved into the double structure that passed over the observation site at 01:40 UTC and eventually exited the camera's field of view approximately 2 h later. No other depletions were observed on this evening before or after this event. This event is illustrated in the sequential images in Fig. 3, where the dark bands traversing the image are the plasma bubbles, or depletions. For this study we analyze in detail the coincident image and GPS data for this night where the single well-identified plasma depletion allows an unambiguous correlation between datasets.

4. GPS data analysis

GPS satellites broadcast very stable dual frequency radio signals at 1575.42 and 1227.6 MHz, called L1 and L2, respectively. These signals are affected by the ionosphere, but are dispersed in a well-understood fashion, which permits users to correct for the ionospheric delay (see, e.g. Hofmann-Wellenhof, 1994) and allows an inde-

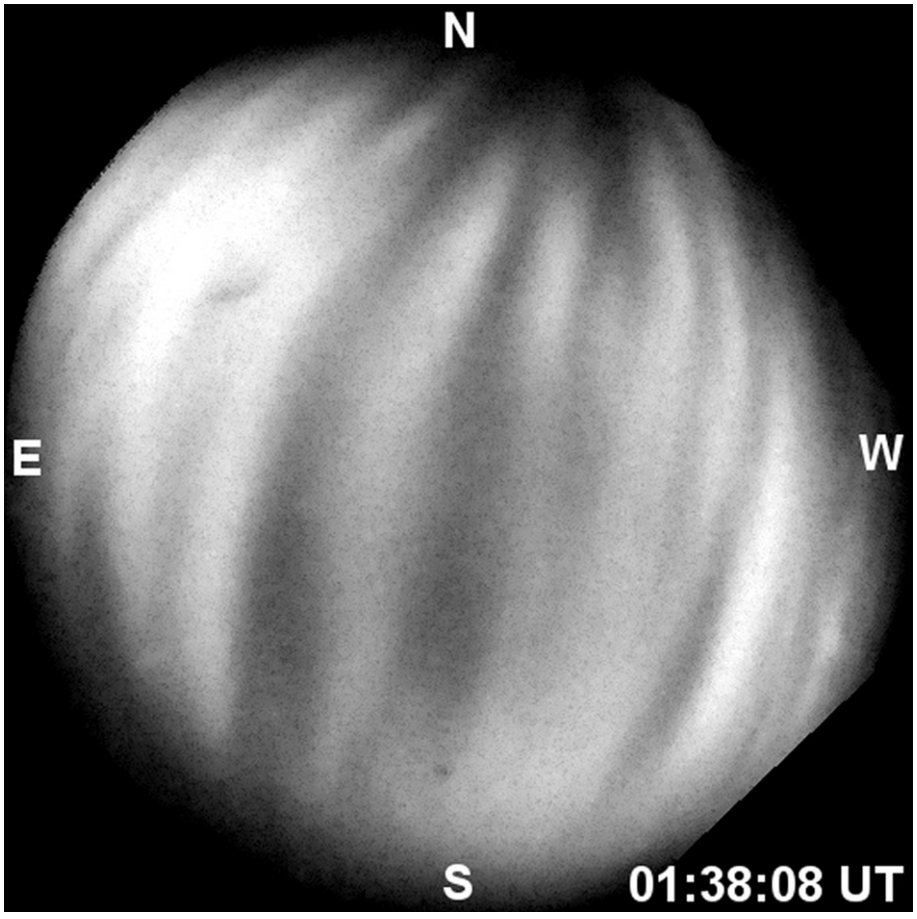

Fig. 2. An example of multiple plasma depletions imaged in the 630 nm airglow emission on the night of September 30 – October 1, 2005. The airglow depletions were observed for 4.8 h from 23:00 to 03:40 UTC from Fazenda Isabel, near Brasilia. The image is shown with the stars removed.

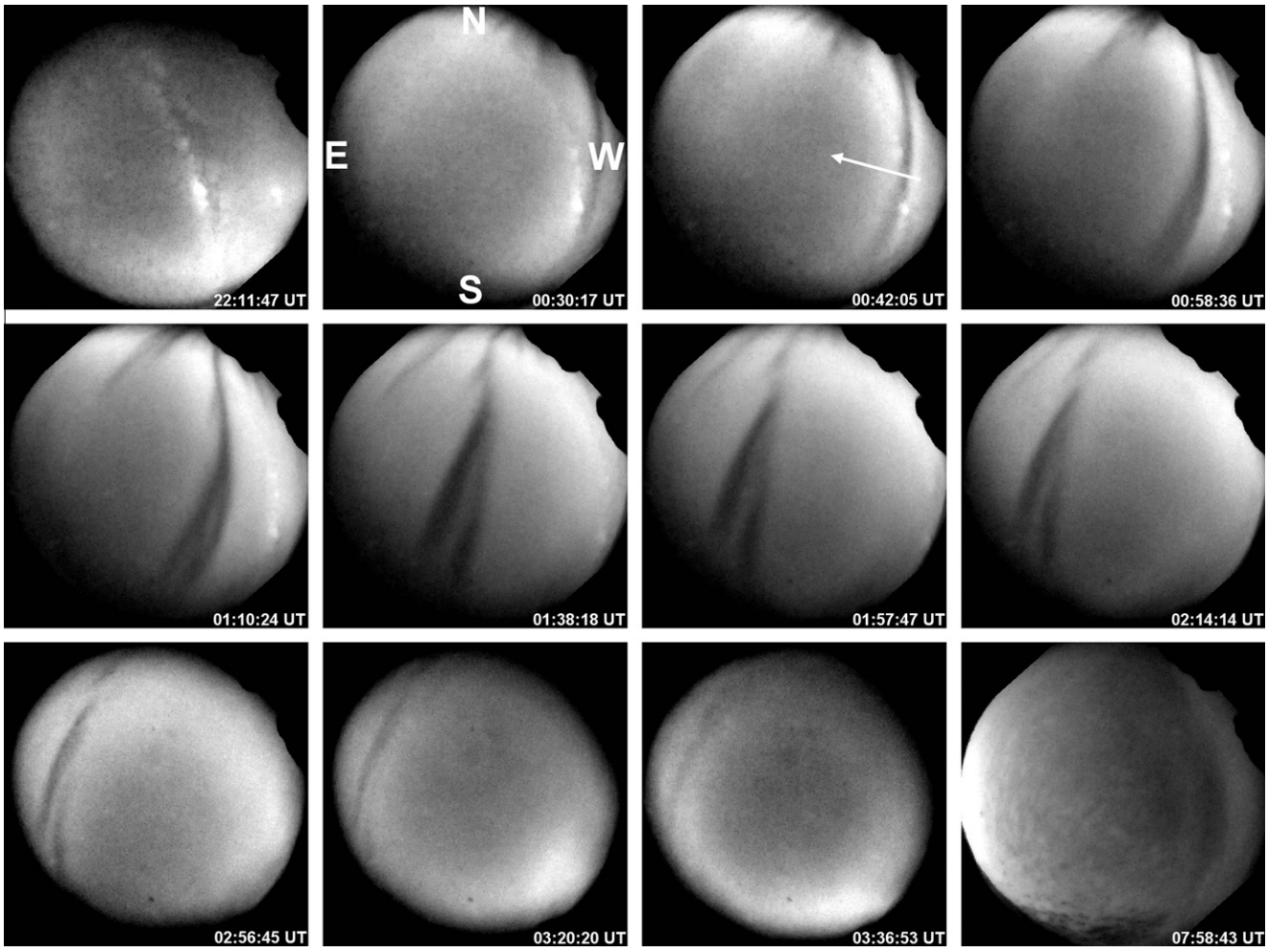

Fig. 3. Sequence of 630 nm airglow images from Fazenda Isabel, near Brasilia, during the night of October 1–2, 2005, from 22:11:47 to 07:58:43 UTC. Note that east is to the left in this image. A single plasma depletion (elongated dark band) is first seen to the west at 00:30:17 UTC. This feature moved eastward (indicated by the arrow) and evolved into the double structure that passed over the observation site at 01:40 UTC and eventually exited the camera field of view approximately 2 h later. The white arrow indicates the drift direction. The images are shown with the stars removed. No other depletions were observed on this evening before or after this event.

pendent determination of the integrated electron content (IEC). Lanyi and Roth (1988) concluded that estimates of the integrated electron content along the receiver-to-satellite line-of-sight estimated from processing dual-frequency GPS signals are as accurate as estimates obtained from the Faraday rotation technique. The integrated electron content (IEC) is calculated from dual frequency GPS data using the relative delay on each carrier. Given carrier phase measurements on each frequency (Φ_1 and Φ_2), the following expression describes the *IEC*:

$$IEC = \left(\Phi_2 - \frac{f_2}{f_1}\Phi_1 + N\right)\frac{f_1^2 f_2}{f_1^2 - f_2}\frac{c}{A} \quad (1)$$

where $A = 40.3\ \mathrm{m^3/s^2}$, c is the speed of light and f_1 and f_2 are the carrier frequencies of L1 and L2 signals. N is a phase ambiguity constant that can be derived from GPS pseudorange data. Note that the IEC measurements are ambiguous because of these phase ambiguities (one for each satellite) and uncalibrated code offsets in the satellites and receivers (transmitter group delay and interfrequency bias). The code biases are constant over long time periods, therefore they do not need to be known to study variations of ionospheric electron content over the course of one satellite pass (Calais et al., 2003).

Each GPS IEC data point is associated with a geographical location, the sub-ionospheric point (SIP), the projection on the surface of the point where the ray path crosses the peak electron density at the time of the GPS observation, usually taken to be between 250 and 450 km altitude (Fig. 4). In this case, the International Reference Ionosphere (IRI) was used to compute the height of the F-layer peak, which for the day of interest was 300 km, shown at the left in Fig. 4 (Bilitza, 2001, 2008). This processing method yields one IEC time series for each ground station/satellite pair. The IEC values are mapped to the zenith using an elevation mapping function $E(\theta)$, which

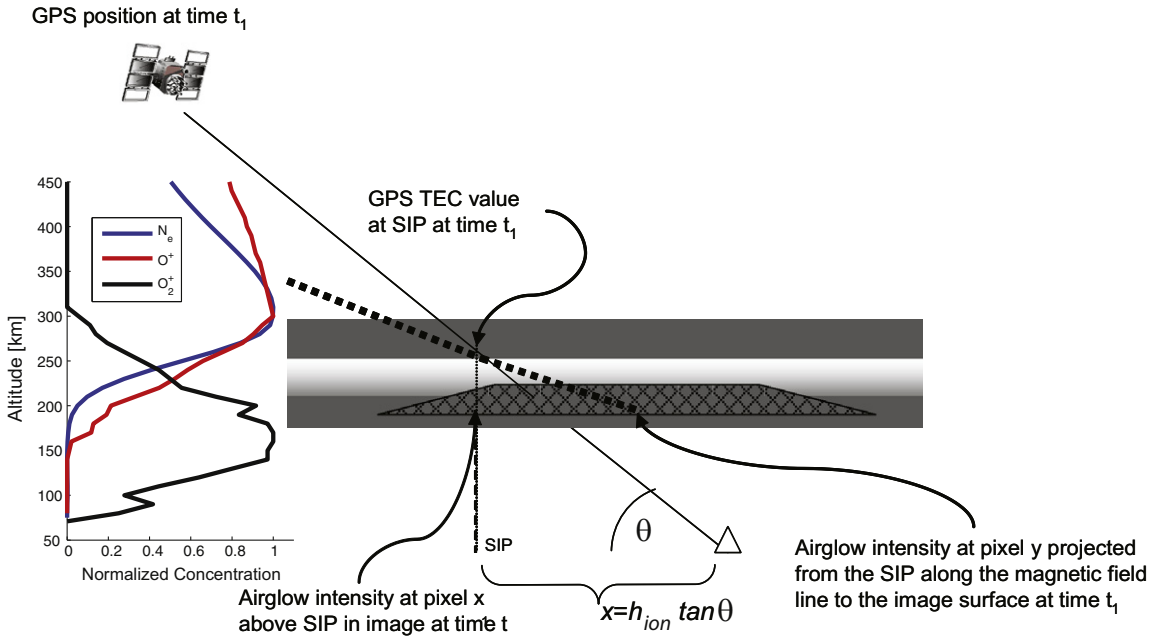

Fig. 4. Schematic illustration of the GPS and airglow measurement geometry. The sub-ionospheric point (SIP) is the location on the ground vertically below where the line of sight pierces the ionosphere at approximately 300 km. The dotted line shows the airglow pixel directly above the SIP. The dashed line shows the projection of the ionospheric pierce point along the magnetic field line to the altitude of the airglow image.

accounts for the different ray path lengths through the atmosphere as the satellite elevation angle θ varies (e.g. Calais et al., 2003; Dautermann et al., 2007 and the references therein):

$$E(\theta) = \sqrt{1 - \frac{\cos(\theta) R_E}{R_E + h_{ion}}} \tag{2}$$

where h_{ion} is the mean ionospheric height and R_E the Earth's radius. The high amplitude long period variations due to daily solar activity are removed using a fourth order polynomial fit to the time series to make the shorter period signals more visible.

Plasma depletions are evident as troughs in the IEC time series shown in Fig. 5. They occur at all sites for satellites PRN4, PRN8, and PRN28. PRN4 has a broader trough, because the line-of-sight is at lower elevation angles than the others, even though a correction was done to map the IEC values to zenith. PRN28 shows two troughs in the IEC. The relative timing of the troughs at the different sites indicates propagation of the depletion to the east. There is a small increase in IEC immediately preceding and following the depletion in the detrended time series due to the detrending process, although the amplitude of this increase may not be reliably represented since the fourth order polynomial was removed from the original TEC time series.

The time of the occurrence of the plasma depletion seen at the different GPS stations is used to determine the propagation velocity of the depletion. The troughs seen at stations ALPA and FAZ1 in Fig. 5a for satellite PRN4 occur earlier than the trough at station TERE. A similar pattern is seen for recordings for satellite PRN8, and for both troughs for satellite PRN28. Fig. 6 shows a map of the location of the sub-ionospheric point at each time sample of the time series, with the color indicating the magnitude of the IEC. The bright blue colors (low IEC values) indicate the points where the IEC dropped sharply. This happened simultaneously for points from ALPA and FAZ1, within the 30 s time resolution of the samples, and at a later time for station TERE. We assume that there was a disturbance propagating perpendicular to a line through the two SIPs where the trough occurred at the same time, and then reached the SIP of the line of sight for station TERE at a later time. We estimate the time difference between the observation of the troughs at ALPA and FAZ1 with respect to the observation at TERE. Then we calculate the perpendicular distance of the SIP at the minimum of the depletion seen at TERE to the line intersecting the SIPs of depletions at ALPA and FAZ1. Since the SIP mapping already takes into consideration the motion of the GPS satellite, the velocity can be determined in this manner without any concern for a Doppler shift in the IEC time series due to the SIP motion, as long as the time series is not filtered in pass bands that would exclude the Doppler shifted signal (Garrison et al., 2007). We compute a velocity for the signals from each of the three satellites, which sample different areas of the ionosphere. Using PRN28, the propagation direction of the depletion is about 80 ± 3 m/s at an azimuth of 73.6°. The velocity was 119 ± 7 m/s at 71.7° using PRN4 (the farthest west traces in Fig. 6) and 101 ± 3 m/s at 79.1° using PRN8 (the center

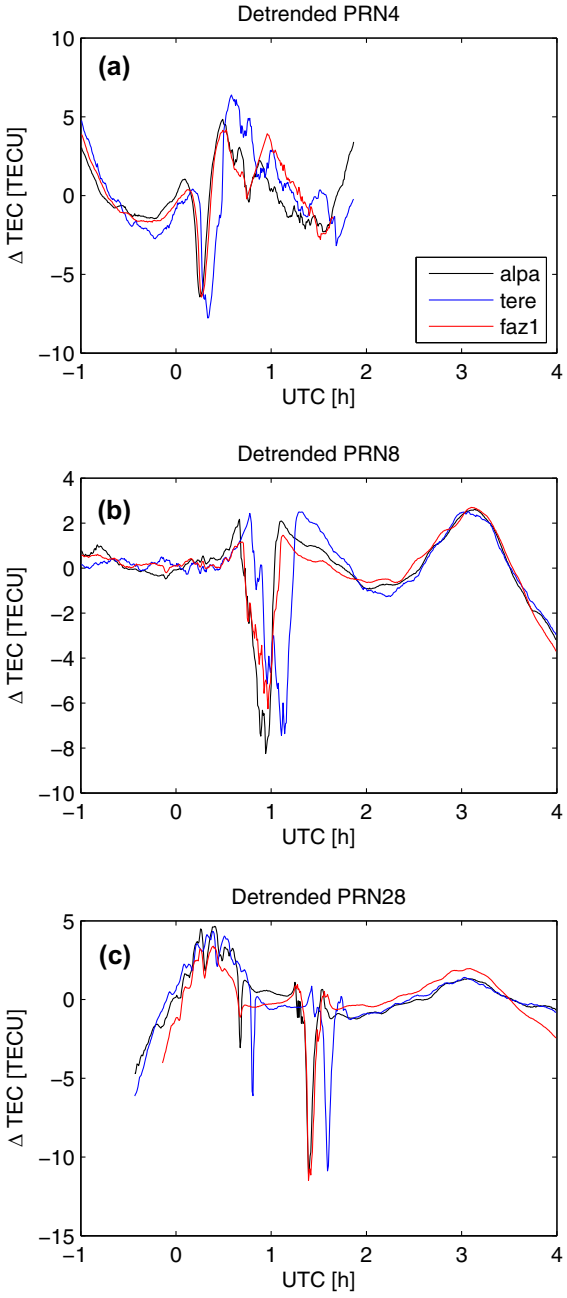

Fig. 5. (a) IEC time series for satellite PRN4 recorded at stations ALPA, TERE, and FAZ1. PRN4 set at about 02:00 UTC. (b) IEC time series for satellite PRN8. (c) IEC time series for satellite PRN28. Two sets of troughs are seen at about 00:45 and 01:30 UTC.

traces). The propagation speed decreases as the disturbance propagates to the east. The disturbance was only present on signals for satellites to the west of the recording array and not to the east (Fig. 6). As seen in the airglow images in Fig. 7, the depletion did propagate east of the array, however the paths and the timing of the other satellite overpasses are such that the line-of-sight does not intersect the depletion.

We also calculate an approximate scintillation index value which we call PS4 (pseudo S4, similar to the ionospheric S4 scintillation index (Yeh and Liu, 1982) for these time series. We use the signal to noise ratio (SNR) recorded on the L2 channel for each satellite-receiver pair, sampled at 30 s. We averaged over 4 min intervals. Usually the S4 index for GPS is calculated using L1 only receivers sampling at 50 Hz or higher, so our measure PS4 results in lower overall values and lower temporal resolution than is typical in studies that use S4. Despite the low resolution, high PS4 index is generally correlated with the IEC depletion, as can be seen in Fig. 8, Figs. 9 and 10. The PS4 scintillation index rises gradually and starts at a later time than the initial ionospheric depletion seen in the IEC from satellite PRN4. In the case of PRN8, because of the sharp decrease in IEC and the low background level of PS4, it is easy to see that the time of the onset of high PS4 is closely correlated with the passage of the eastern edge of the depletion over the site. For PRN28, the PS4 index does not detect the structure of the first trough for FAZ1 and APLA. For the second trough, the onset of high PS4 is abrupt at station ALPA, and less so at FAZ1 and TERE, but also appears to correlate with the initial decrease in IEC rather than the minimum in IEC. These subtleties in the relative timing of the depletion seen in the PS4 time series and in the IEC time series give different estimates of the motion of the depletion. Using the cross-correlation of the onset of high PS4 to calculate the depletion velocity gives a velocity of 180 m/s at an azimuth of 74.4° from PRN8 and a velocity of 65.4 m/s at an azimuth of 73.6° from PRN28. These velocities vary greatly from those estimated from IEC, but since different scale-sizes are being observed here, the velocity measurements obtained from cross-correlation are not necessarily required to be the same as the one obtained from GPS IEC or airglow data (especially during active development of the irregularities, see Beach and Kintner (2001) and the references therein).

5. Airglow and GPS data comparison

The airglow and GPS data are compared in order to confirm the detection of the plasma depletions, to compare their characteristics, and to investigate any height sensitivity of the measurements. OI emission at 630.0 nm is a sensitive indicator of F-layer vertical motions and plasma density because emission is enhanced when the F-layer moves downward (Pimenta et al., 2007). Image data were first calibrated using the known star field. The stars were then removed and each image was unwarped onto a 1500×1500 km uniformly spaced grid assuming an emission altitude of 280 km. There is an overall drift of the intensity that increases with time as the background level increases over the course of the evening. The airglow is expected to detect variations that occur slightly below the peak electron density in the ionosphere, which is assumed to be the height of maximum sensitivity of the GPS observations. In order to make a time-domain comparison, a time series is constructed of the airglow intensity at the airglow image pixel directly below the point where the GPS line of sight intersects a surface at the height of the F-layer

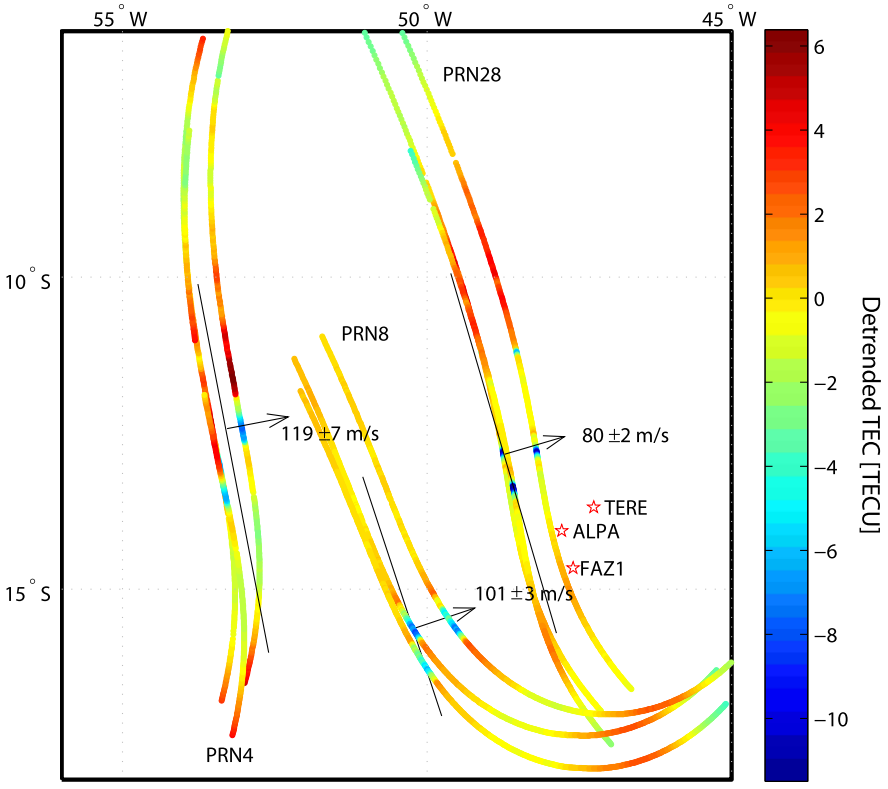

Fig. 6. Map showing the trace of the sub-ionospheric point (the location on the ground of the piercing point of the satellite-receiver line-of-sight where it intersects the F-layer ionosphere). The amplitude of the detrended signal is shown in color. Traces for those satellites that have no obvious disturbance in the IEC are shown in gray. PRN27 data (not shown) has some evidence of a low amplitude reduction in TEC that may be associated with the depletion.

peak. The geometric mapping (Fig. 4) at time t is made using the relation:

$$|\mathbf{x}(t)| = h_{ion} \tan(\phi(t)) \quad (3)$$

where h_{ion} is the hypothesized height of the F-layer assumed for the IEC, ϕ is the elevation angle of the GPS satellite, and $\boldsymbol{x}$ is the resulting distance from the airglow imager site. The intensity of the pixel at $\boldsymbol{x}$ is assigned to time t in the airglow time series.

Fig. 11 shows the airglow time series where the height of maximum sensitivity h_{ion} is set to 300 km for PRN8 and PRN28. The trajectory for PRN4 overlies the airglow image where it is obstructed near the horizon, so it is not shown. PRN28 and PRN8 show a similar shape for the depletion observed in the time series from airglow and that observed in the GPS IEC, but with the airglow depletion occurring earlier. The overall time scale and shape of the depletion is very similar in the two types of time series. The two troughs seen in the GPS IEC time series for PRN28 are confirmed in the airglow images. The images indicate that the first trough is a smaller depletion with less poleward extent than the main depletion. There is some indication of an even smaller depletion prior to that at approximately 00:30 UTC.

The increase in IEC at the edges of the depletion noted earlier in the GPS time series also appears to be common to the airglow time series. Ledvina and Makela (2005) made a comparison of Wide Area Augmentation Satellite (WAAS) scintillation measurements and airglow images and interpreted that greater scintillation occurs on the leading and trailing walls of the plasma bubbles, compared to the interior, and attribute this to the larger background electron density at the walls. Higher background electron density is one interpretation of the rise in TEC preceding and following the trough seen prominently in Figs. 8–10. These observations provide support for a steep gradient in electron density at the edges of the plasma bubble being the cause of scintillation. However, in this case the scintillation continues throughout the duration of the depletion.

The relative size of the peaks between the airglow and GPS observations provides a useful indication of the strength of the airglow depletions in terms of electron density. The ratio of the CCD intensity units to TEC units for the depletion gives a correspondence between the two types of observation. 214–300 intensity units were observed for 7.4–11.4 TECU for satellite PRN8 and PRN28. These observations at two different elevation angles give an approximate relation of 0.035–0.038 TECU/CCD intensity units.

There is a resolvable difference in the time of the disturbance measured with the two data types, as can be seen by comparing the solid and gray lines in Fig. 11. The disturbance appears earlier on the airglow traces. We check the sensitivity to our assumptions about the F-layer height

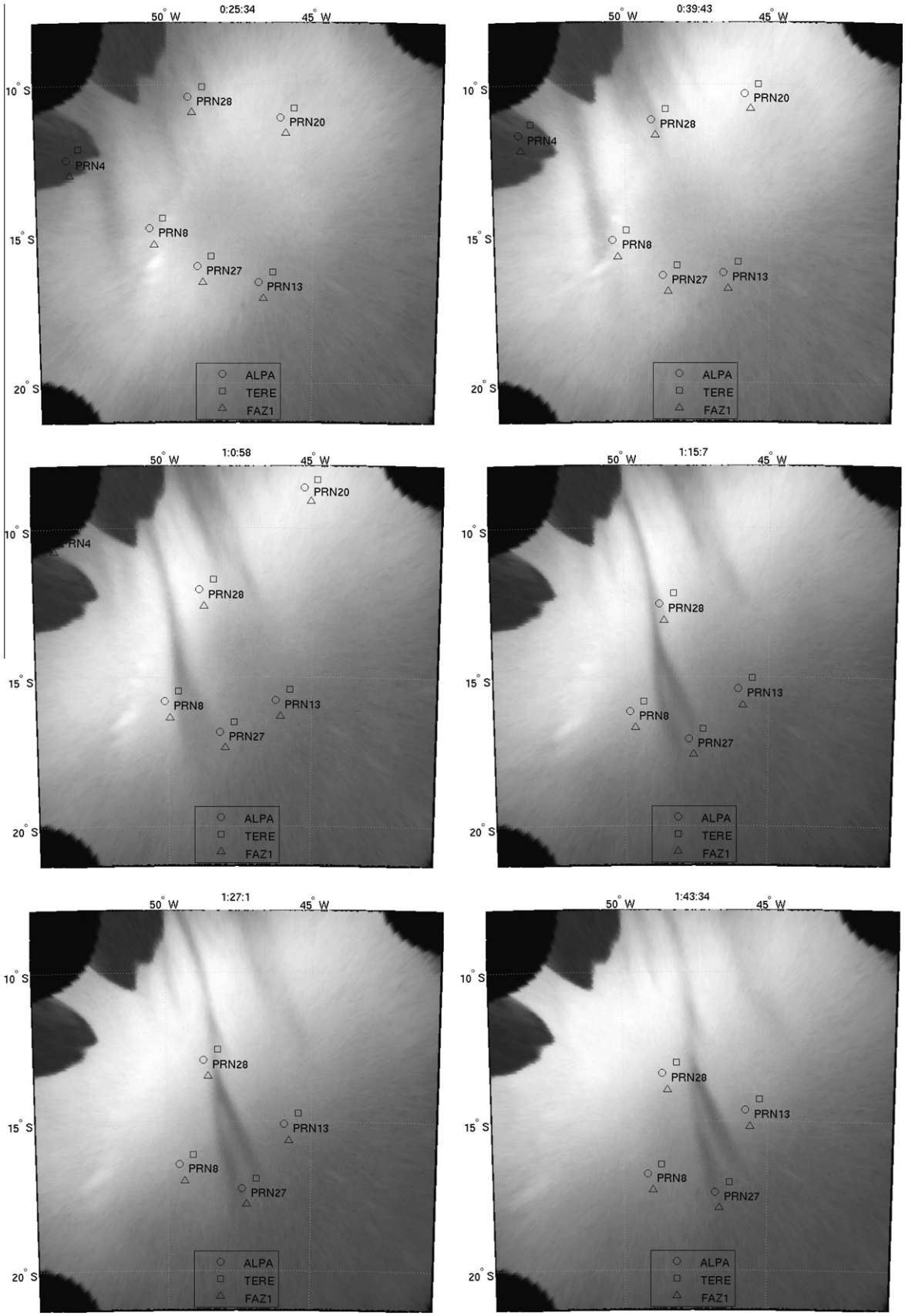

Fig. 7. SIP locations superimposed on airglow images for times where velocities are estimated. Note that no depletions are detected in the GPS IEC time series for PRN13, PRN20, PRN23 because of the unfavorable geometry where the depletion does not cross the path of the GPS line-of-sight. The detection of a depletion in the GPS IEC for PRN27 is ambiguous.

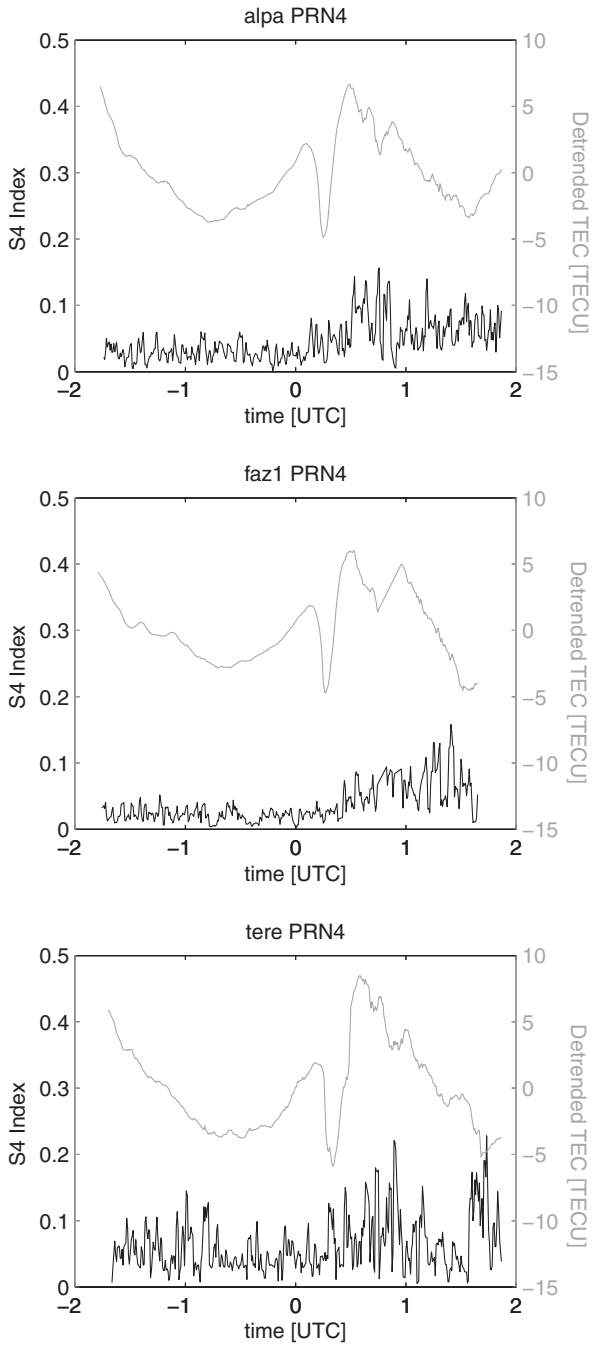

Fig. 8. An approximate PS4 pseudo-scintillation index (lower trace in each panel) computed from the signal to noise ratio of the signals sampled at 30 s from satellite PRN4 recorded at stations ALPA, FAZ1, and TERE. The PS4 index rises at approximately the same time as the IEC depletion occurs, however it appears to precede the IEC depletion for ALPA and lag the depletion for FAZ1.

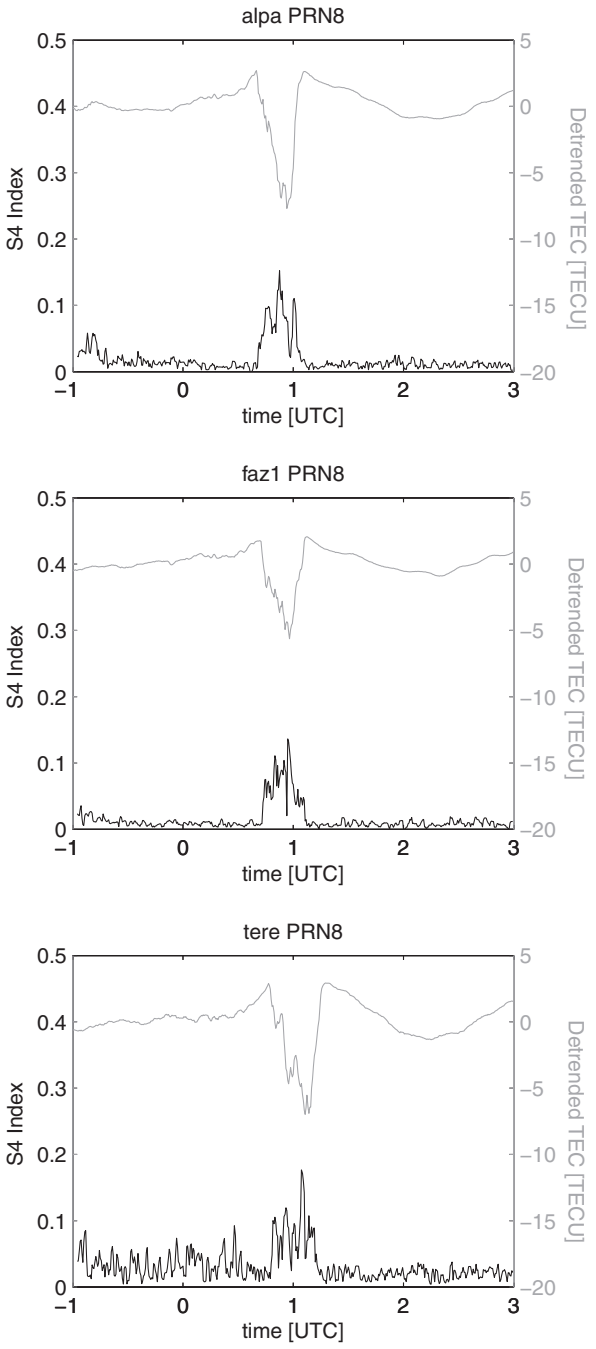

Fig. 9. PS4 scintillation index (lower trace in each panel) computed from the signal to noise ratio of the signals from satellite PRN8 recorded at stations ALPA, FAZ1, and TERE. The PS4 index rises abruptly at same time as the steep decrease in IEC as the eastern wall of the depletion passes over the site.

for the GPS TEC by assigning the height h_{ion} to 280 km, below the IRI model F-layer peak. The depletion in the airglow data pixel directly below the IEC ionospheric pierce point is mapped to a slightly later time in the time series (dashed line in Fig. 11) but still well ahead of the time of the depletion in the GPS time series. If the airglow data were actually measuring what was occurring at 300 or 280 km, the depletions would occur at the same time as those in the GPS IEC. One can interpret from the delay that the airglow is sensitive to a significantly lower height than the GPS IEC observations, and lower than that predicted by the IRI model.

The fact that the GPS IEC is not aligned in time with the depletion in the pixel directly below in the airglow image implies that there is a tilt in the plasma bubble. Vertical shear in the eastward plasma drift velocity

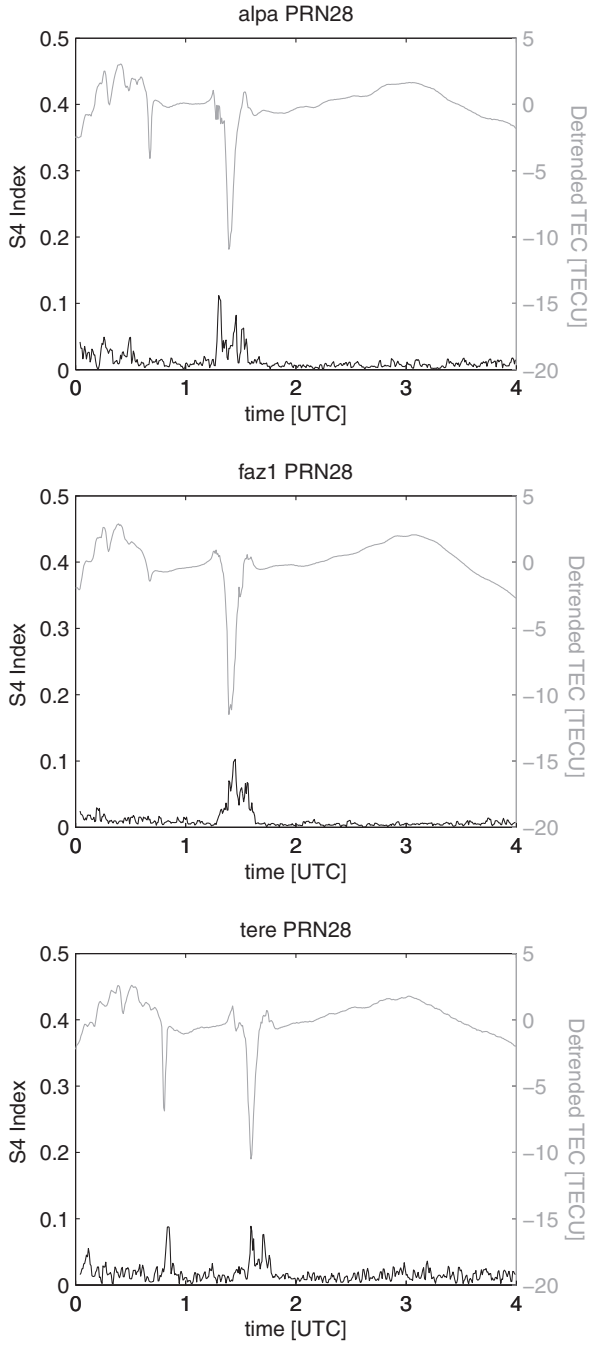

Fig. 10. PS4 scintillation index (lower trace in each panel) computed from the signal to noise ratio of the signals from satellite PRN28 recorded at stations ALPA, FAZ1, and TERE. The PS4 is clearly correlated with the second trough, but does not detect the first trough in the IEC at all sites.

would cause the depletion to appear later in the GPS IEC time series if it were displaced to the west at the IEC altitudes relative to where it is seen in the airglow images. The time offset is less for the PRN28 SIP, which is farther to the east than the PRN8 SIP (Fig. 6). This would indicate that there is less tilt at the later time when the depletion intersects the line of sight with PRN28. This is counter to other observations made of depletion tilt. For example, Makela and Kelley (2003), made estimates of velocity shear from narrow field airglow images, which showed a westward tilt in the plasma bubbles. Their observations from a narrow field imager aimed south towards the equator projected the airglow depletions presumed to be occurring at different latitudes to a map of the depletions as a function of height at the equator. They calculated a vertical shear of 0.1 m/s/km for the drift velocity difference from 500 to 900 km altitude. The tilt in general has been shown in radar data and in narrow field airglow imagery to be greater at later times in the evening (Kelley et al., 2003). However, with the combined airglow and GPS IEC we show the existence of tilt at a single location independently of an assumed mapping of the effects of ESF from the equator to lower latitude regions along high conductivity magnetic field lines. This combination of GPS and airglow observations is complementary to optical emission observations from satellites such as the Global Ultraviolet Imager (GUVI) (Kelley et al., 2003; McDonald et al., 2006) and 774.1 nm airglow measurements because they demonstrate the tilt structure below 350 km, which cannot be seen by these other techniques.

We can explain the delay in time if we assume it is due to the fact that over the height difference between the GPS IEC and airglow sensitivity, the depletion is continuous along the magnetic field line. The magnetic field line has an inclination of approximately 24° at this latitude at an altitude of 300 km. We map the GPS IEC ionospheric pierce point along the direction of the magnetic field line to the assumed height of the airglow emission layer (dashed line in Fig. 4, schematically shown in Fig. 12). This pixel is then assigned the same time as the GPS IEC observation to construct an airglow time series for comparison (Fig. 13). We find an airglow emission layer height of 265 km gives the closest match in time between the GPS IEC and airglow depletion for both satellites PRN8 and PRN28. Thus, assuming a constant height for the TEC measurement, we have used the correspondence between the airglow and GPS data to resolve the height of the airglow emission layer (as opposed to assuming the airglow emission layer height in the previous discussion).

The comparison confirms that the signal seen in the GPS time series are plasma depletions observed in the airglow, and therefore that the GPS IEC appears to sample properties of the plasma bubble observations at the same scale and with the same associated features as the airglow. The PS4 index, on the other hand, does not coincide in time consistently with either the edges or the deepest part of the depletion. This motivates future investigations with both S4 and local array GPS IEC measurements to further probe the timing of plasma bubble features at different scales. GPS IEC provides a means to estimate, or calibrate, the magnitude of the plasma density depletion within the airglow image. Finally, when used in combination with airglow it provides additional information on the relative heights of the F-layer and airglow emission layer.

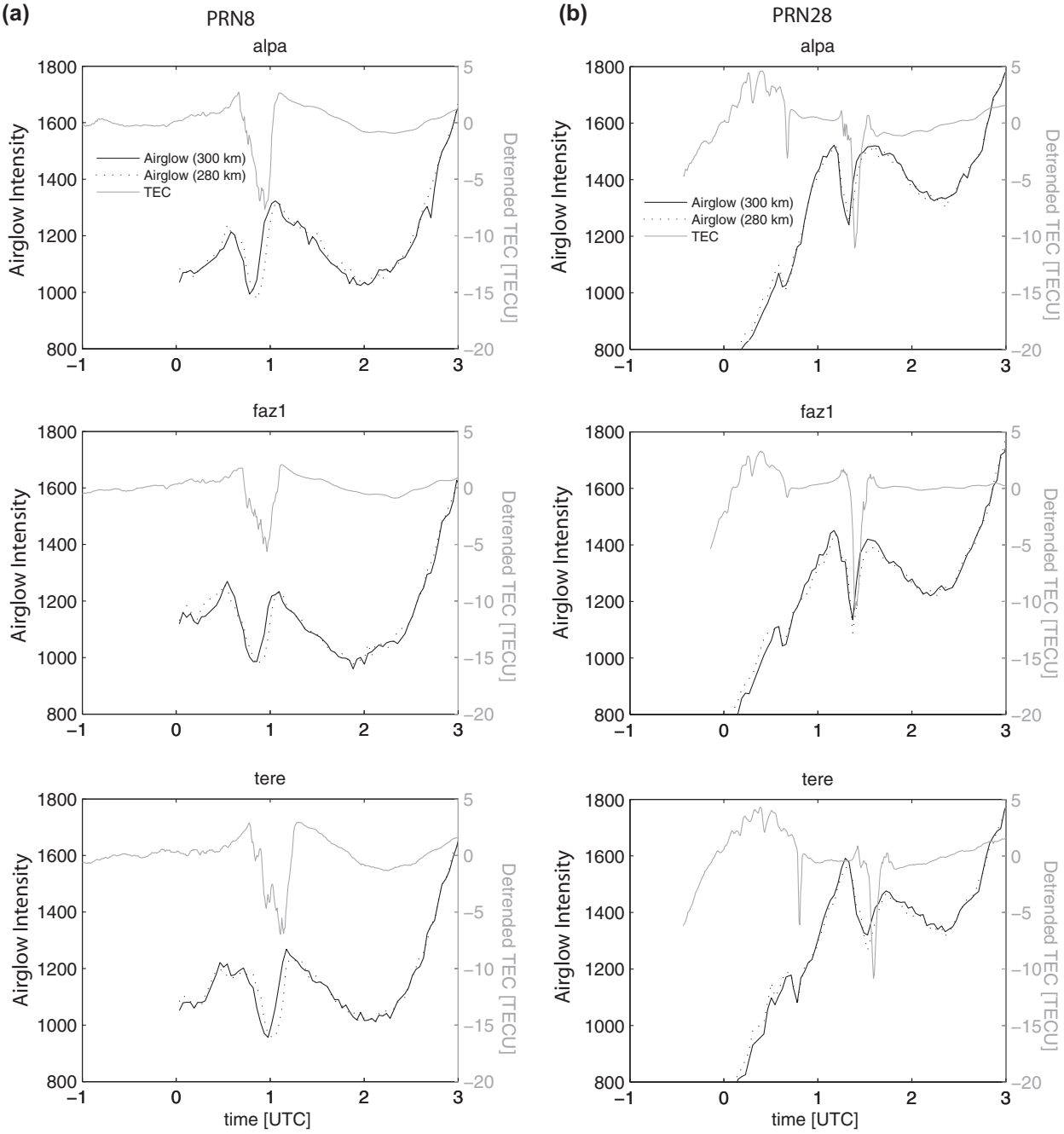

Fig. 11. (a) Detrended GPS IEC for satellite PRN8 and intensity extracted from the 630.0 nm airglow images (black) mapped to 300 km (gray) and 280 km (dashed) at the SIP corresponding to each site. (b) IEC and airglow time series for satellite PRN28. With this mapping, the depletion occurs earlier in the airglow than the GPS time series. This implies a tilt to the plasma plume.

6. Drift velocity of the plasma depletion

Two methods are used to determine the motion of the depletions in time and space using the airglow data and the GPS IEC data. The method for calculating the velocity from GPS IEC was described in a previous section (Fig. 6). The GPS IEC data show a propagation velocity at an azimuth of 70–74°, roughly from west to east, with speeds decreasing from 119 to 80 m/s over the 1000 km visible from the array. The 630 nm image data have been analyzed to determine the motion of the depletions (direction and speed) and their variability during the course of the night using the following technique. Well-developed 2-D Fourier spectral analysis methods are used to determine the horizontal scale sizes of the features (Garcia et al., 1997). The drift motions of the depletions are measured at various positions in the image corresponding to different apex altitudes. For this study, we have focused on drift measurements at the ionospheric penetration points for direct comparison with GPS data. Drift velocities were estimated

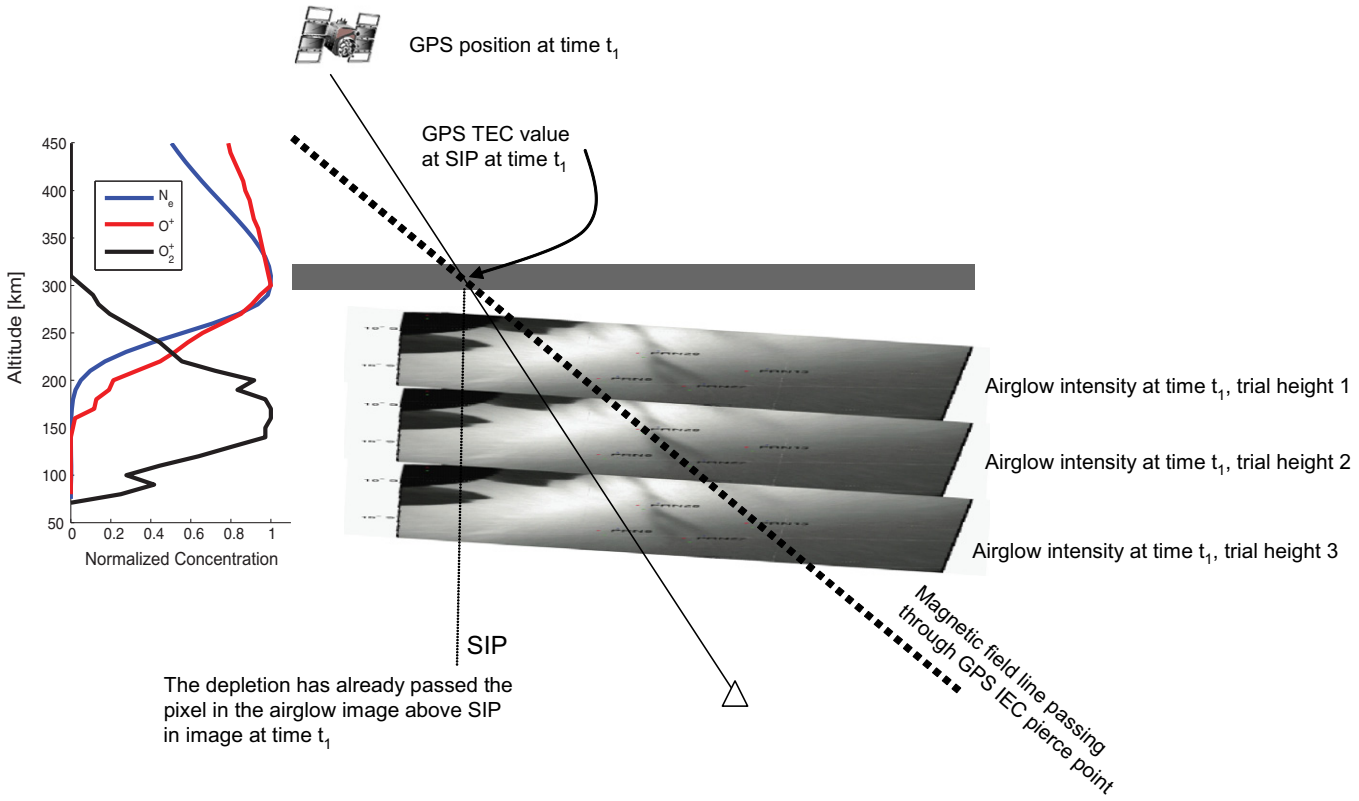

Fig. 12. Schematic representation of the projection along magnetic field lines from the IEC value at the F-layer height to the height of the airglow image. This illustrates graphically the approach used for determining the height of airglow emission to be 265 km, by adjusting the height until the depletion location coincides with the intersection of the magnetic field line.

by selecting four consecutive images that encompass the time when the depletion in the image is vertically below the GPS SIP. We then define several features on the depletion (e.g. edge or finer scale structure) close to this point and determine their average motion during this time (typically 10 min). These velocities are directly comparable to the GPS velocities that are shown in Fig. 6, and are given in Table 2. The velocity of 80 ± 3 m/s is calculated for PRN28 at 300 km altitude based on the GPS IEC for the time period spanned by the depletions at the three stations. The airglow images provide velocities that decrease from 85 ± 5 to 72 ± 4 m/s for that time period from 1:23 to 1:40 UTC. The average velocity retrieved from the GPS agrees with the airglow drift velocity to within the ~7 m/s error bars. This agreement is also shown at the locations in the images of the PRN4 SIP and the PRN8 SIP. The airglow observation comparable to that retrieved from PRN4 was taken at a slightly different time in order to be above the obstructions near the horizon. The velocities measured by the GPS array are within the error bars of the airglow estimates.

The horizontal drift is estimated from the airglow image in the same manner for the entire time period from 0:15 to 3:30 UTC (Fig. 14) for a point within the main depletion at 15°S latitude. After crossing the array, the depletion has continued to decrease its eastwards horizontal drift velocity to as low as 20 m/s. The GPS IEC velocities are also shown on this figure at the locations within the image of the PRN4, PRN8, and PRN28 SIPs, and are quite consistent with the airglow observations despite the fact that they are made at different latitudes where the magnetic field lines may be at higher altitudes.

The decrease in zonal velocity as a function of time is also visible in a keogram (cf. Taylor et al., 2009). Here the intensity from an east–west cross-section through the airglow images is plotted as a function of time (Fig. 15). In this geometry, for a depletion that is traveling nearly west to east, a coherent structure shows up as a dark linear feature in the keogram, with a slope that corresponds to the velocity. The curving of this feature after about 1 h UTC indicates a decrease in velocity as the depletion moves to the east. The east–west distance of the sub-ionospheric-point from Fazenda Isabel and the time that the depletion is seen by each satellite is indicated in Fig. 15 superimposed on the keogram. For example, the SIP for PRN8 is approximately 350 km west of Fazenda Isabel and the depletion is seen on that record at about 01:00 UTC. This is near the same time that the depletion is seen in the keogram from the 630.0 nm airglow imager. Similarly for the other two satellites SIP points. An interesting thing to note is the separation of the depletion into two structures after passing the PRN8 SIP.

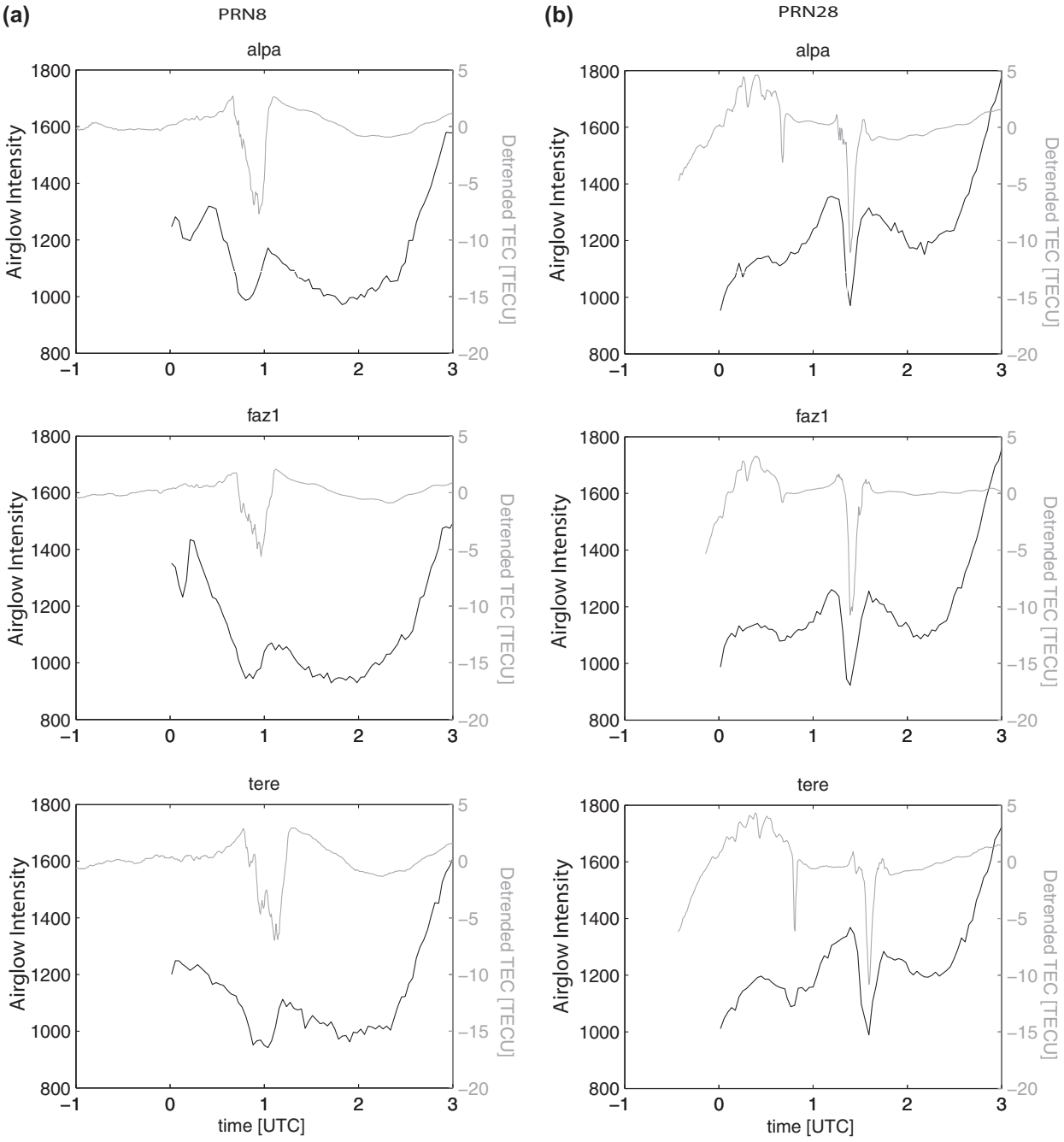

Fig. 13. (a) Detrended GPS IEC for PRN8 (gray) and intensity extracted from the 630 nm airglow images (black) with the ionospheric pierce point mapped to 265 km along the magnetic field line. (b) IEC and airglow time series for satellite PRN28. With this mapping, the airglow depletion occurs simultaneously with that in the GPS time series. This implies a continuous extension of the depletion along the field lines to lower latitude and altitude.

7. Discussion and conclusions

In this study we were able to track the evolution of a plasma bubble using combined GPS integrated electron content, an approximate pseudo-scintillation index GPS PS4, and 630.0 nm airglow observations. While depletion signals have been observed in the past with GPS, this is the first study where multiple datasets have been used to quantitatively correlate specific features in airglow imagery and GPS local arrays to show their correspondence, and to determine drift velocity for direct comparison. Previous work with short baseline (70 m) correlation of GPS signal S4 index to determine velocity (Kil et al., 2000) did not provide conclusive evidence of agreement with other observation types. If PS4 is a reasonable approximation for S4, then this may possibly indicate that the PS4 signal is not as accurate as IEC for determining the velocity of features of the scale that are observed in airglow. It is not necessary to assume mapping of depletions along magnetic field lines to estimate drift velocity. In this case, the plasma depletion developed early in the evening of October 1. The drift velocity was estimated from PRN4 while it was in its

Table 2
Velocity of depletions measured with airglow and GPS. Depletion time for the airglow is the time of the central frame of the four frame sequence used for determining the velocity when the named site was within the depletion. Depletion time for the GPS TEC is the time of the minimum in the TEC.

Satellite	Site	Airglow		TEC	
		Velocity [m/s]	Depletion time [UTC]	Velocity [m/s]	Depletion time [UTC]
PRN4	ALPA, FAZ1	112 ± 6	0:14:57	119 ± 7	0:15:00
	TERE	111 ± 5	0:29:06		0:19:48
PRN8	ALPA, FAZ1	105 ± 6	0:57:26	101 ± 3	0:57:00
	TERE	99 ± 5	01:11:35		1:06:18
PRN28	ALPA, FAZ1	85 ± 5	01:23:27	80 ± 3	1:23:24
	TERE	72 ± 4	01:40:01		1:35:24

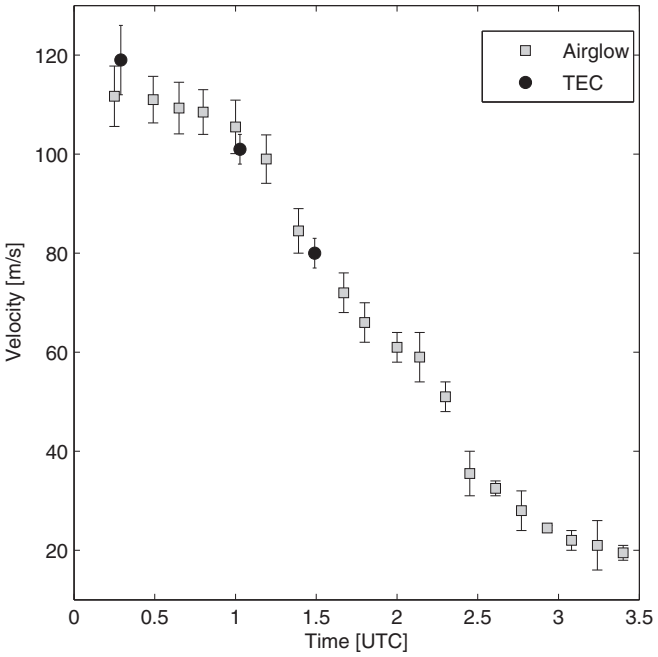

Fig. 14. Velocity of the major depletion observed the night of October 1–2 measured from airglow images (squares), and GPS IEC (circles). The location in the image where the velocity was estimated is within the depletion as it moves, so is taken to be further east with increasing time. Local Time is UTC-3.

development stage and confined spatially to the northwestern part of the image, and at several later times after the depletion was more mature. The southernmost extent of the depletion in the airglow images increases, in agreement with the general understanding of the increase in latitudinal extent along the magnetic field line with time as the depletion increases in height at the equator. West of the observation site near Brasilia, the velocity of the plasma bubble was 119 ± 7 m/s based on the GPS IEC array data, which was consistent with the value of 112 ± 6 m/s retrieved from the airglow imager. The velocity decreased as the depletion moved to the east, to a value 80 ± 3 m/s estimated from GPS and of 72–85 ± 5 based on the airglow data. Both the GPS and airglow were able to discern the slowing of the depletion as it crossed the observation site.

Visualizing the entire spatio-temporal domain with an airglow imager clearly shows the evolution of the plasma bubbles, and it is obvious that GPS cannot provide that level of spatial resolution. Also, it is clear from Fig. 6 that sometimes an unfavorable geometry prevents a depletion from being visible in the GPS IEC time series. However, the GPS observations have the advantage that they are not affected by clouds or moonlight, so there is the potential of getting more information on the frequency of occurrence and statistics of the depletion events from GPS than from airglow. Also, GPS poses a low cost alternative for extending the continuity of observations between the limited number of ionospheric observatories. This is necessary in order to address questions about the formation location of the different depletions and when they are triggered. By combining information from GPS and airglow, it is possible to get an idea of the strength of the airglow depletions in absolute IEC units in the ionosphere, and it is possible to extract information about the height sensitivity of these features.

Previous work, in particular Weber et al. (1996) and Valladares et al. (2004), looked at the characteristics of GPS scintillation and IEC to predict the occurrence of depletions strong enough to produce scintillation as a function of latitude and local time. These studies used sparse GPS data sets where the timing of depletion passages over the SIPs could not unambiguously be related to westward tilt of the depletion or eastward drift velocity because of the large separations between sites. The stage of depletion development along magnetic field lines was interpreted based on the relative timing between S4 and IEC (Weber et al., 1996). This study investigates the relation of GPS observations to spatial characteristics of depletions observed in airglow data without making assumptions about the instantaneous mapping of depletions along field lines so that the time evolution and extent with latitude is unambiguous. We provide quantitative estimates of velocity that give valid explanations of the timing of depletion occurrence. Adding in the assumption of depletion development along field lines, we additionally are able to determine the relative height of sensitivity of the GPS IEC and airglow emissions.

The local estimates of velocity eliminate errors due to the changing shape and characteristics of the plume as it extends poleward, as opposed to determining drift velocities by combining observations from 2 different satellite look angles or combining observations from sites with large longitudinal separation. We observe large

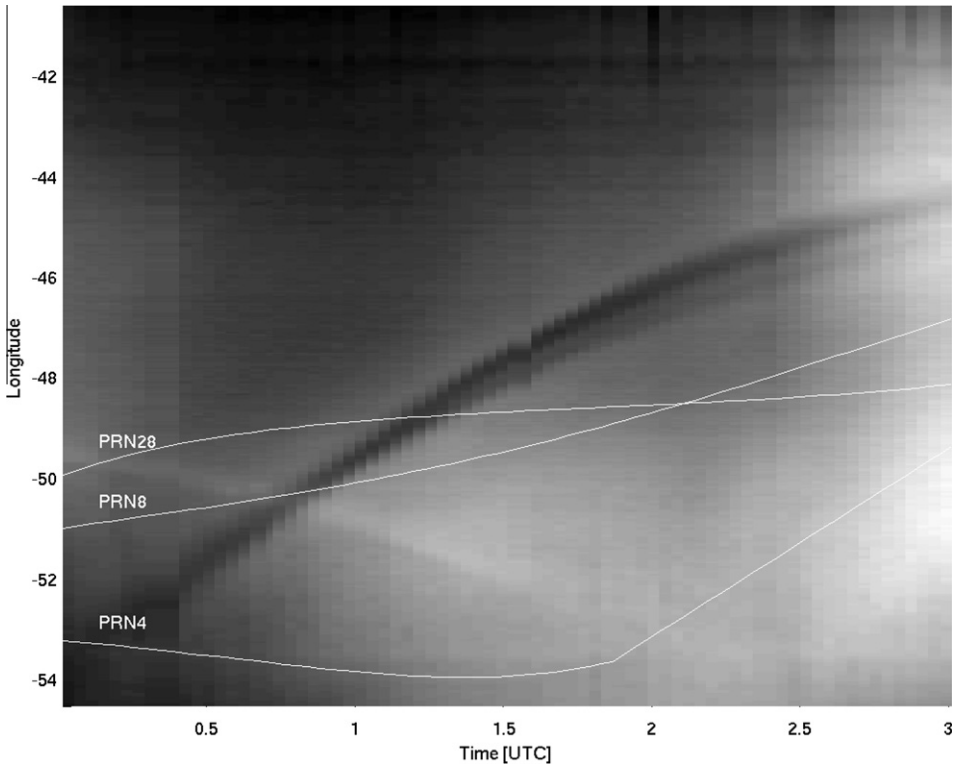

Fig. 15. 630.0 nm airglow image keogram at 14.67°S latitude. Longitude axis indicates distance east from imager location at Fazenda Isabel. The location of the satellite SIPs are shown with the white lines, though the SIP may be at a slightly different latitude.

horizontal gradients in drift velocity. For example, there is a large difference in velocity (seen both in GPS and airglow) between the time the depletion passes over the PRN8 SIP and the PRN28 SIP. This is consistent with a downward electric field generated by the F-region dynamo that is decreasing over time causing a reduction in the E × B plasma drift.

Previous work suggested that scintillation is simultaneous with the IEC depletion when the depletion is mature or frozen and moves over the observation site, as opposed to a developing depletion. There is some support for this, because the PS4 index scintillation begins well after the IEC depletion at the location of the PRN4 SIP, where the depletion is broad and limited in extent to north of 15°S in the airglow image, so could be considered the development phase. The PS4 scintillation is near simultaneous with the IEC depletion when it passes over the PRN8 and PRN28 SIPs and judging by its fixed southern limit could be considered in the frozen stage. These ideas should be confirmed with high sample rate true S4 observations.

The implications of this work for understanding the development of ESF and forecasting scintillation due to ESF are the following:

(1) We have shown the direct correspondence between IEC depletions and characteristics of depletions seen in horizontal airglow images, with very consistent observations of scale, amplitude, drift velocity and timing. The velocity accuracy was demonstrated to be better than 7 m/s.
(2) Lack of depletion observations from some GPS viewing angles does NOT indicate the absence of a depletion, demonstrated by this case where motion of the GPS satellites in the northeast quadrant by chance did not sample the depletion which was present there.
(3) We have shown that local GPS array observations are useful for investigating the time and latitude dependence of the growth of depletions along field lines, which in many studies is assumed to be nearly instantaneous from the equator to the lower latitude limit. Theoretically, the westward tilt of depletions is dependent on the ratio of equatorial F-region and off-equatorial E-region Pedersen conductivities, so the combined GPS and airglow observations that show evidence of tilt may lead in the future to a better understanding of the link between off-equatorial conductivity and ESF. Since estimates of origin time and location of depletions are often based on estimates of tilt, this work also may lead to better description of the conditions where ESF is generated.

Acknowledgements

This data was collected with funding through Dave Fritts from NASA contract NNH04CC67C, "Experimental and Modeling Studies of Potential Gravity Wave Seeding of Plasma Dynamics at Equatorial Latitudes". The Utah State all-sky image measurements and data analyses were supported by a sub-contract from NWRA Inc as part

of the NASA LWS grant (PI D. Fritts). We gratefully acknowledge the help of Fernanda Sao Sabbas, Eurico de Paula and Institute Nacional de Pesquisas Espaciais for logistical coordination of the fieldwork. We thank Paytsar Muradyan for help with preliminary analysis of the GPS data. The National Space Science Data Center International Reference Ionosphere was used to generate electron density profiles.

Appendix A. Supplementary data

Supplementary data associated with this article can be found, in the online version, at doi:10.1016/j.asr.2010.09.025.

References

Abdu, M.A. Outstanding problems in the equatorial ionosphere-thermosphere electrodynamics relevant to spread F. Journal Of Atmospheric And Solar-Terrestrial Physics 63, 869–884, 2001.

Abdu, M.A., Kherani, E.A., Batista, I.S., de Paula, E.R., Fritts, D.C., Sobral, J.H.A. Gravity wave initiation of equatorial spread F/plasma bubble irregularities based on observational data from the SpreadFEx campaign. Annales Geophysicae 27, 2607–2622, 2009.

Basu, S., Kudeki, E., Basu, S., Valladares, C.E., Weber, E.J., Zengingonul, H.P., Bhattacharyya, S., Sheehan, R., Meriwether, J.W., Biondi, M.A., Kuenzler, H., Espinoza, J. Scintillations, plasma drifts, and neutral winds in the equatorial ionosphere after sunset. Journal of Geophysical Research 101, 26795–26809, 1996.

Beach, T.L., Kintner, P.M. Simultaneous Global Positioning System observations of equatorial scintillations and total electron content fluctuations. Journal of Geophysical Research-Space Physics 104, 22553–22565, 1999.

Beach, T.L., Kintner, P.M. Development and use of a GPS ionospheric scintillation monitor. IEEE Transactions on Geoscience and Remote Sensing 39 (5), 918–928, 2001.

Bilitza, D. International Reference Ionosphere 2000. Radio Science 36, 261–275, 2001.

Bilitza, D. The international reference ionosphere. NSSDC, 2008.

Calais, E., Haase, J.S., Minster, J.B. Detection of ionospheric perturbations using a dense GPS array in Southern California. Geophysical Research Letters 30, doi:10.1029/2003GL017708, 2003.

Chen, W.S., Lee, C.C., Liu, J.Y., Chu, F.D., Reinisch, B.W. Digisonde spread F and GPS phase fluctuations in the equatorial ionosphere during solar maximum. Journal of Geophysical Research-Space Physics 111, doi:10.1029/2006JA011688, 2006.

Dautermann, T., Calais, E., Haase, J., Garrison, J. Investigation of ionospheric electron content variations before earthquakes in southern California, 2003–2004. Journal of Geophysical Research 112, B02106, doi:10.1029/2006JB004447, 2007.

de Paula, E.R., Kantor, I.J., Sobral, J.H.A., Takahashi, H., Santana, D.C., Gobbi, D., de Medeiros, A.F., Limiro, L.A.T., Kil, H., Kintner, P.M., Taylor, M.J. Ionospheric irregularity zonal velocities over Cachoeira Paulista. Journal of Atmospheric and Solar-Terrestrial Physics 64, 1511–1516, 2002.

Fritts, D. C., Abdu, M. A., Batista, B. R., Batista, I. S., Batista, P. P., Buriti, R., Clemesha, B. R., Dautermann, T., de Paula, E. R., Fechine, B. J., Fejer, B. G., Gobbi, D., Haase, J., Kamalabadi, F., Kherani, E. A., Laughman, B., Lima, P. P., Liu, H.-L., Medeiros, A., Pautet, P.-D., Riggin, D. M., Rodrigues, F. S., São Sabbas, F., Sobral, J. H. A., Stamus, P., Takahashi, H., Taylor, M. J., Vadas, S. L., Vargas, F., Wrasse, C. M. Overview and summary of the Spread F Experiment (SpreadFEx). Annales Geophysicae 27, 2141–2155, doi:10.5194/angeo-27-2141-2009, 2009.

Garcia, F.J., Kelley, M.C., Makela, J.J., Huang, C.S. Airglow observations of mesoscale low-velocity traveling ionospheric disturbances at midlatitudes. Journal of Geophysical Research-Space Physics 105, 18407–18415, 2000a.

Garcia, F.J., Kelley, M.C., Makela, J.J., et al. Mesoscale structure of the midlatitude ionosphere during high geomagnetic activity: airglow and GPS observations. Journal of Geophysical Research-Space Physics 105, 18417–18427, 2000b.

Garcia, F.J., Taylor, M.J., Kelley, M.C. Two-dimensional spectral analysis of mesospheric airglow image data. Applied Optics 36, 7374–7385, 1997.

Garrison, J.L., Lee, S.C.G., Haase, J.S., Calais, E. A method for detecting ionospheric disturbances and estimating their propagation speed and direction using a large GPS network. Radio Science 42 (6), doi:10.1029/2007RS003657, 2007.

Hofmann-Wellenhof, B. Global Positioning System: Theory and Practice. Springer-Verlag, New York, 1994.

Huang, C.S., Kelley, M.C. Nonlinear evolution of equatorial spread F.1. On the role of plasma instabilities and spatial resonance associated with gravity wave seeding. Journal of Geophysical Research-Space Physics 101, 283–292, 1996a.

Huang, C.S., Kelley, M.C. Nonlinear evolution of equatorial spread F.2. Gravity wave seeding of Rayleigh–Taylor instability. Journal of Geophysical Research-Space Physics 101, 293–302, 1996b.

Kelley, M.C. The Earth's Ionosphere. Academic Press, San Diego, 1989.

Kelley, M.C., Kotsikopoulos, D., Beach, T., Hysell, D., Musman, S. Simultaneous global positioning system and radar observations of equatorial spread F at Kwajalein. Journal of Geophysical Research-Space Physics 101, 2333–2341, 1996.

Kelley, M.C., Makela, J.J., Paxton, L.J., Kamalabadi, F., Comberiate, J.M., Kil, H. The first coordinated ground- and space-based optical observations of equatorial plasma bubbles. Geophysical Research Letters 30, doi:10.1029/2003GL017301, 2003.

Kil, H., Kintner, P.M., de Paula, E.R., Kantor, I.J. Global Positioning System measurements of the ionospheric zonal apparent velocity at Cachoeira Paulista in Brazil. Journal of Geophysical Research-Space Physics 105, 5317–5327, 2000.

Kil, H., Kintner, P.M., de Paula, E.R., Kantor, I.J. Latitudinal variations of scintillation activity and zonal plasma drifts in South America. Radio Science 37, doi:10.1029/2001RS002468, 2002.

Klobuchar, J.A. Ionospheric time delay effects on earth space propagation, in: Jursa, A.S. (Ed.), Handbook of Geophysics and the Space Environment. U.S. Air Force, Washington, D.C, pp. 1084–1088, 1985 (Chapter 10.8).

Lanyi, G.E., Roth, T. A comparison of mapped and measured total ionospheric electron-content using global positioning system and beacon satellite-observations. Radio Science 23, 483–492, 1988.

Ledvina, B.M., Makela, J.J. First observations of SBAS/WAAS scintillations: using collocated scintillation measurements and all-sky images to study equatorial plasma bubbles. Geophysical Research Letters 32, doi:10.1029/2004GL021954, 2005.

Makela, J.J., Kelley, M.C. Field-aligned 777.4-nm composite airglow images of equatorial plasma depletions. Geophysical Research Letters, 30, 2003.

Makela, J.J., Ledvina, B.M., Kelley, M.C., Kintner, P.M. Analysis of the seasonal variations of equatorial plasma bubble occurrence observed from Haleakala, Hawaii. Annales Geophysicae 22, 3109–3121, 2004.

Martinis, C., Mendillo, M. Equatorial spread F-related airglow depletions at Arecibo and conjugate observations. Journal of Geophysical Research-Space Physics 112 (A10310), doi:10.1029/2007JA012403, 2007.

Maruyama, T. A diagnostic model for equatorial spread F.1. Model description and application to electric field and neutral wind effects. Journal of Geophysical Research 93, 14611–14622, 1988.

Maruyama, T., Matuura, N. Longitudinal variability of annual changes in activity of equatorial spread F and plasma bubbles. Journal of Geophysical Research 89, 903–912, 1984.

McDonald, S.E., Basu, S., Groves, K.M., Valladares, C.E., Scherliess, L., Thompson, D.C., Schunk, R.W., Sojka, J.J., Zhu, L. Extreme longitudinal variability of plasma structuring in the equatorial ionosphere on a magnetically quiet equinoctial day. Radio Science 41, doi:10.1029/2005RS003366, 2006.

Mendillo, M., Baumgardner, J. Airglow characteristics of equatorial plasma depletions. Journal of Geophysical Research-Space Physics 87, 7641–7652, 1982.

Mendillo, M., Lin, B.S., Aarons, J. The application of GPS observations to equatorial aeronomy. Radio Science 35, 885–904, 2000.

Mendillo, M., Tyler, A. Geometry of depleted plasma regions in the equatorial ionosphere. Journal of Geophysical Research-Space Physics 88, 5778–5782, 1983.

Pimenta, A.A., Sahai, Y., Bittencourt, J.A., Rich, F.J. Ionospheric plasma blobs observed by OI 630 nm all-sky imaging in the Brazilian tropical sector during the major geomagnetic storm of April 6–7, 2000. Geophysical Research Letters 34, doi:10.1029/2006GL028529, 2007.

Rodrigues, F.S., de Paula, E.R., Abdu, M.A., Jardim, A.C., Iyer, K.N., Kintner, P.M., Hysell, D.L. Equatorial spread F irregularity characteristics over Sao Luis, Brazil, using VHF radar and GPS scintillation techniques. Radio Science 39, RS1S31, doi:10.1029/2002RS002826, 2004.

Taylor, M.J., Bishop, M.B. All-sky measurements of short-period waves imaged in the Oi(557.7 nm), Na(589.2 nm) and near-infrared oh and O-2(0, 1) nightglow emissions during the Aloha-93 campaign. Geophysical Research Letters 22, 2833–2836, 1995.

Taylor, M.J., Eccles, J.V., LaBelle, J., Sobral, J.H.A. High resolution OI (630 nm) image measurements of F-region depletion drifts during the Guara campaign. Geophysical Research Letters 24, 1699–1702, 1997.

Taylor, M. J., Pautet, P.-D., Medeiros, A. F., Buriti, R., Fechine, J., Fritts, D. C., Vadas, S. L., Takahashi, H., São Sabbas, F. T. Characteristics of mesospheric gravity waves near the magnetic equator, Brazil, during the SpreadFEx campaign. Annales Geophysicae 27, 461–472, doi:10.5194/angeo-27-461-2009, 2009.

Terra, P.M., Sobral, J.H.A., Abdu, M.A., Souza, J.R., Takahashi, H. Plasma bubble zonal velocity variations with solar activity in the Brazilian region. Annales Geophysicae 22, 3123–3128, 2004.

Tinsley, B.A., Christen, A.b., Bittenco, J., Gouveia, H., Angreji, P.D., Takahash, H. Excitation of oxygen permitted line emissions in tropical nightglow. Journal of Geophysical Research 78, 1174–1186, 1973.

Tsunoda, R.T. Control of the seasonal and longitudinal occurrence of equatorial scintillations by the longitudinal gradient in integrated E-region Pedersen conductivity. Journal of Geophysical Research-Space Physics 90, 447–456, 1985.

Valladares, C.E., Basu, S., Groves, K., Hagan, M.P., Hysell, D.L., Mazzella, A.J.J., Sheehan, R.E. Measurement of the latitudinal distributions of total electron content during equatorial spread F events. Journal of Geophysical Research 106, 29133–29152, doi:10.1029/2000JA000426, 2001.

Valladares, C.E., Sheehan, R., Basu, S., Kuenzler, H., Espinoza, J. The multi-instrumented studies of equatorial thermosphere aeronomy scintillation system: climatology of zonal drifts. Journal of Geophysical Research-Space Physics 101, 26839–26850, 1996.

Valladares, C.E., Villalobos, J., Sheehan, R., Hagan, M.P. Latitudinal extension of low-latitude scintillations measured with a network of GPS receivers. Annales Geophysicae 22, 3155–3175, 2004.

Weber, E.J., Basu, S., Bullett, T.W., Valladares, C., Bishop, G., Groves, K., Kuenzler, H., Ning, P., Sultan, P.J., Sheehan, R.E., Araya, J. Equatorial plasma depletion precursor signatures and onset observed at 11° south of the magnetic equator. Journal of Geophysical Research-Space Physics 101, 26829–26838, 1996.

Whalen, J.A. The equatorial anomaly: its quantitative relation to equatorial bubbles, bottomside spread F, and the E × B drift velocity during a month at solar maximum. Journal of Geophysical Research 101, 29125–29132, 2001.

Yeh, K.C., Liu, C.H. Radio wave scintillations in the ionosphere. Proceedings of the IEEE 70, 324–360, 1982.

Zalesak, S.T., Ossakow, S.L., Chaturvedi, P.K. Nonlinear equatorial spread F – The effect of neutral winds and background Pedersen conductivity. Journal of Geophysical Research-Space Physics 87, 151–166, 1982.